

Strain-induced bi-thermoelectricity in tapered carbon nanotubes

L.A.A. Algharagholy^{1,3}, T. Pope², and C.J.Lambert¹

¹*Department of Physics, Lancaster University, Lancaster, United Kingdom*

³*Department of Physics, College of Science, University of Sumer, Al Riffae, Thi Qar, Iraq*

Abstract

We show that carbon-based nanostructured materials are a novel testbed for controlling thermoelectricity and have the potential to underpin the development of new cost-effective environmentally-friendly thermoelectric materials. In single-molecule junctions, it is known that transport resonances associated with the discrete molecular levels play a key role in the thermoelectric performance, but such resonances have not been exploited in carbon nanotubes (CNTs). Here we study junctions formed from tapered CNTs and demonstrate that such structures possess sharp transport resonances near the Fermi level, whose energetic location can be varied by applying strain, resulting in an ability to tune the sign of their Seebeck coefficient. These results reveal that tapered CNTs form a new class of bi-thermoelectric materials, exhibiting both positive and negative thermopower. This ability to change the sign of the Seebeck coefficient allows the thermovoltage in carbon-based thermoelectric devices to be boosted by placing CNTs with alternating-sign Seebeck coefficients in tandem.

Keywords:

Keywords: thermopower, molecular electronics, carbon nanotubes

Introduction

The design of efficient thermoelectric materials for converting waste heat directly into electricity is a research topic of intense current interest¹⁻¹⁶. Although inorganic semiconductors have received much attention and are the favoured solution for high-temperature thermoelectrics,^{14,15} recent attention has focussed on the advantages of organic thermoelectrics^{1-13,16}, which are sustainable, non-toxic and could underpin the design of efficient flexible materials for scavenging waste heat from the human body or the ambient environment. It has been demonstrated both experimentally and theoretically that at the level of a single molecule, the

Seebeck coefficient S can range in magnitude from ca. 1 to 50 $\mu\text{V}/\text{K}$, depending on the position of intra-molecular energy levels relative to the work function of metallic electrodes^{2,3}. The latter can be tuned using an electrostatic gate¹⁰, an electrochemical gate¹⁶, varying the chemical composition¹, varying the lengths of single-molecule lengths, changing the terminal groups which bind a molecule to the electrodes molecules⁴⁻⁸, or by tuning the interaction between two neighbouring fullerenes⁹.

A key factor in determining the thermoelectric performance of a molecular junction is the presence of transport resonances close to the Fermi level. In an early theoretical work,¹² it was predicted that resonances induced by quantum interference effects could be mechanically tuned by the rotation of side groups attached to a molecular backbone leading to high thermopower (ie Seebeck coefficient) and high thermoelectric figure of merit. Interference-induced transmission nodes¹³ are also predicted to be advantageous for thermoelectricity. More recently, mechanical tuning of thermopower in helicene molecular junctions has been predicted¹⁷.

Recent experiments and theory of C_{60} -based thermoelectricity⁹ and other studies^{2,3,10} showed that C_{60} is a thermoelectric material, with a robust negative Seebeck coefficient, which remains negative even in the presence of an applied pressure. More recently it was demonstrated experimentally and theoretically that the sign of the Seebeck coefficient of the endohedral fullerene $\text{Sc}_3\text{N}@C_{80}$,¹⁸ could be varied by application of pressure. This “bi-thermoelectric” behaviour is unprecedented and demonstrates that a single material can exhibit a Seebeck coefficient of either sign, without doping and without a change of chemical composition. Bi-thermoelectricity is important, because compatible materials with Seebeck coefficients of opposite signs are needed to boost the thermovoltage in tandem devices. Therefore it is of interest to identify other classes of materials which may exhibit this effect.

The above unusual behaviour of endohedral fullerenes stimulated us in the present paper to examine the potential of carbon nanotubes (CNTs) for bi-thermoelectricity. The above experiments are consistent with the fact that the thermoelectric properties of a molecular junction depend on the magnitude and derivative of the transmission at the Fermi level of the electrodes,^{19,20}

$$S = - \frac{\pi^2 k_B^2 T}{3e} \left. \frac{d \ln T(E)}{dE} \right|_{E=E_F} \quad (1)$$

where $T(E)$ is the junction transmission, which is dependent on electron energy E , k_B is the Boltzmann constant, T is the average temperature of the junction, and e is the charge of the electron. Equation (1) demonstrates that if the slope of $\ln T(E_F)$ can be tuned mechanically, then a material could exhibit bi-thermoelectricity. This means that CNTs whose electronic structure is sensitive to axial strain are potential candidates for bi-thermoelectricity. To demonstrate that

this is indeed the case, we explore the electrical, thermoelectrical and mechanical properties of tapered carbon nanotube junctions (TNJs), which (see fig. 1) consist of a small diameter central nanotube connected at each end to larger diameter nanotubes. Such structures are of interest, because the larger nanotubes can be contacted to external reservoirs both electrically and mechanically and therefore be used to inject and collect electrons to and from the central CNT and also to exert an external force on the central CNT. Furthermore the presence of the narrow neck increases the local strain caused by a given axial force²¹. In what follows, we examine how the imposition of axial strain affects the thermoelectric properties of TNJs and demonstrate that TNJs are indeed a new class of bi-thermoelectric materials.

As examples, we analyse TNJs, which consist of a central (3,3), (4,4), or (5,5) CNT attached to two larger (6,6) CNT leads, as shown in figure 1 (right). As discussed in ^{22,23}, such structures can be obtained by starting from a bilayer nanoribbon such as that shown in the left figure and removing lines of atoms (such as those coloured blue) from the edges of the upper and lower ribbons and then allowing the edges to reconstruct to maximise sp_2 bonding. We refer to the final relaxed structure as a ‘sculpturene’. Figure 1a shows an example of a starting structure, which we relaxed to obtain the tapered CNT shown in figure 1b.

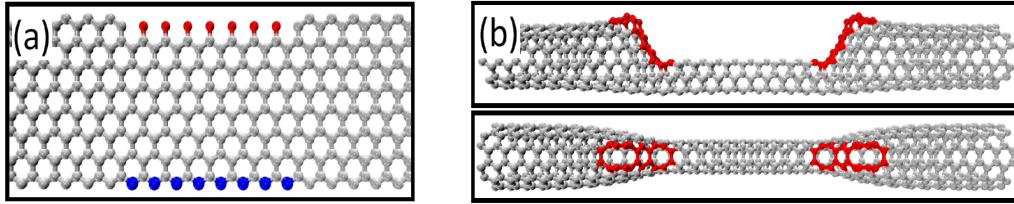


Figure 1. (a): The left figure shows zigzag graphene nanoribbon, ZGNR, with the two edge types. The upper edge (red) shows the β termination, and the lower edge (blue) shows the α termination. (b): The right figure shows a relaxed supercell of the sculpturene system with two (6,6) CNT leads and a central (3,3) scatterer. The regions containing 5 and 7 membered rings are highlighted in red.

Method

To obtain the relaxed structures, we used the SIESTA implementation of density functional theory (DFT) to optimise the structures using the local density approximation (LDA) with the Ceperley-Alder exchange correlation functional and double zeta polarized (DZP) basis set^{24,25}. The initial bi-layer strips are relaxed until the forces on the atoms are minimised to below 0.03 eV/Å, which is sufficient to form the sculpturene nanostructures. Once the final sculpturenes were relaxed, the SIESTA DFT Hamiltonian was combined with the Gollum transport code²⁶, to obtain the low-bias electron transmission coefficient $T(E)$ for electrons of energy E passing from the larger diameter (6,6) CNT on the left, through the scattering region formed by the TNJ to the larger diameter (6,6) CNT on the right.

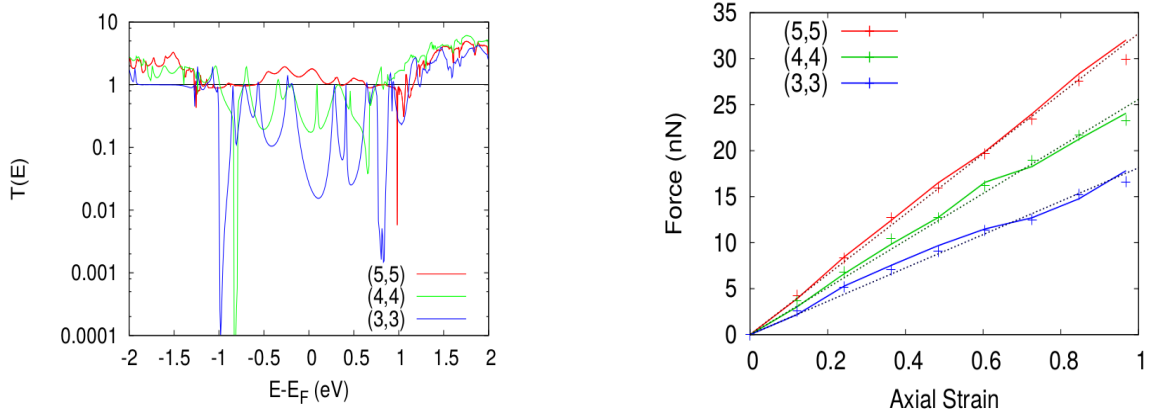


Figure 2 (a): The zero bias transmission coefficients $T(E)$ of the systems in 1b. (b): Absolute value of the force acting on the left (solid lines) and right (points) leads for each system as a function of the axial strain. The axial strain ϵ is defined as the stretching distance divided by the overall length of the junction ($L_j \sim 24.8 \text{ \AA}$). In each case, a linear fit (dotted lines) is obtained and the slope is used to evaluate the surface Young's modulus (Y_s).

Results

Figure 2a shows the electron transmission coefficient $T(E)$ for each of the three structures studied. In the case of the (5,5) TNJ, the transmission around the Fermi energy remains above unity, suggesting that only one transport channel is significantly suppressed, whereas in the narrower (3,3) and (4,4) TNJs, the transmission rarely exceeds unity, indicating that both transport channels are suppressed. Indeed, we note that the conductance, $G = G_0 T(E_F)$, drops significantly as the scatterer is made thinner, following the trend $G_{5,5} = 1.7G_0$, $G_{4,4} = 0.18$ and $G_{3,3} = 0.02G_0$ for the (5,5), (4,4), and (3,3) TNJs respectively. Figure 2a reveals the existence of narrow destructive interference features in $T(E)$ around $E-E_F = \pm 1$ eV in the (4,4) and (3,3) TNJs, which are caused by localized states around the defective regions containing 5 and 7-membered rings. Since they are well away from the Fermi energy, they do not affect the conductance of the junction. Instead, the presence of distinctive resonances in the transmission curves within this energy range shows that scattering from the contacts between the TNJs and (6,6) electrodes leads to Breit-Wigner-type resonances.

To compute the effect of strain on these systems, we stretch the TNJs in the longitudinal direction. To impose this strain, we start from the unstretched sculpture, move the (6,6) leads at either end away from the scatterer by 1.5 \AA and then after restricting the leads to their new positions, relax the TNJ until the forces on the atoms in the TNJ are below 0.03 eV/\AA . We repeat the procedure for a series of (6,6) lead positions until the system reaches breaking point (at a lead separation $> 24 \text{ \AA}$), at which point the junction ruptures. To calculate the force acting on the lead after stretching, we sum the longitudinal Hellmann-Feynman forces on each atom in the lead and

take the average. Figure 2b shows the forces acting on each of the (6,6) leads as they are stretched in the longitudinal direction.

In the limit of weak coupling to the electrodes, transmission peaks occur when the energy E of a transmitted electron lies close to an eigenenergy E_n of the scattering region. Therefore the transmission peaks are expected to move closer together as the junction is stretched and the level spacing decreases. However the opposite effect has also been seen in carbon systems under strain. Here, the force modifies the energies in the system and adds a term to the momentum operator of the Hamiltonian. This so-called pseudo-magnetic effect causes the transmission peaks to moving further apart under strain^{27,28,29}.

In our case, to describe qualitatively the strain-related behaviour of transmission peaks, we fit a simple model of non-interacting Breit-Wigner resonances to the transport curves. For a symmetric structure, a Breit-Wigner resonance is described by the formula, $T_i(E) = 4\Gamma_i^2 / [(E - \epsilon_i)^2 + 4\Gamma_i^2]$. Therefore in the presence of many such resonances, we approximate the transmission coefficient by the following expression

$$T(E) = \sum_i A_i T_i(E) \quad (2)$$

where A_i is a fitting parameter representing the amplitude of the i th Breit-Wigner resonance. Figure 3 (a) shows the transmission coefficient of the first five stretched configurations of the (3,3) TNJ (black) compared equation (2) (Red).

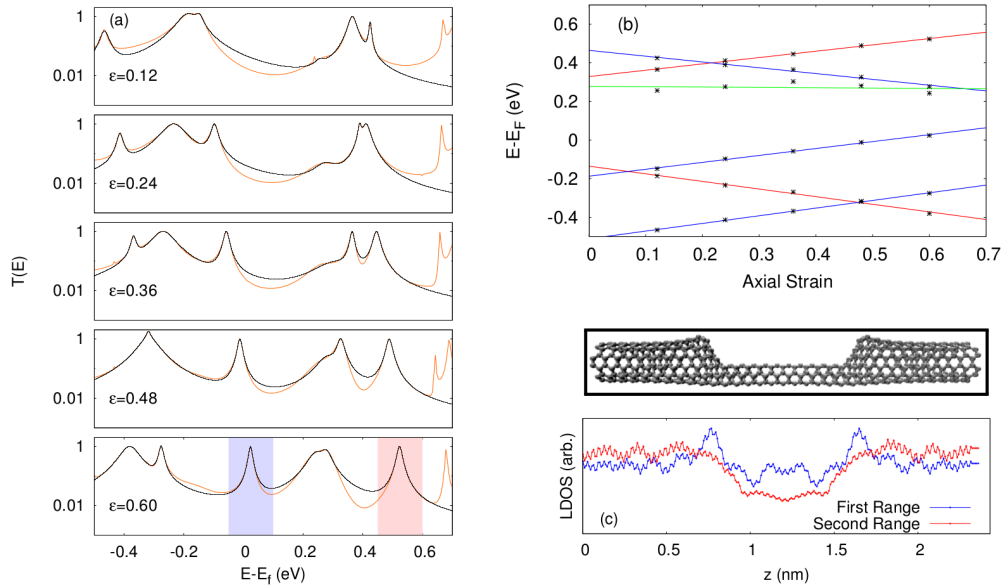


Figure 3. (a) Transmission coefficient against energy for the (3,3) TNJ under axial strain (orange) and the Breit-Wigner fit (Black). The shaded regions in the lower figure represent the energy range used in the LDOS calculations shown in the lower right subfigure. (b) Energies of transmission peaks for the (3,3) TNJ versus axial strain (black). The red, green and blue lines represent the trajectory of the Breit-Wigner peaks evaluated by performing linear fits to the energy values of the peaks. (c) Averaged local density of states per axial distance for the fully stretched (3,3) TNJ for a range of energies to capture the blue ($E-E_F=-0.05$ to $E-E_F=0.1$) and red ($E-E_F=0.45$ to $E-E_F=0.6$) peaks showing that the blue peak is fully delocalised along the length of the junction and the red peak is localised on the (6,6) leads. For reference, the junction structure is shown above the graph.

Fig 3b shows the peak positions ε_i at a series of axial strains, obtained by fitting to the six peaks nearest to the Fermi energy, using a non-linear least-squares Marquardt-Levenberg fitting algorithm. The calculated parameters are presented in the Appendix. In Fig. 3b, as a guide to the eye, these are connected by straight lines, which are coloured depending on the direction the peak moves as a function of axial strain; red for peaks that move away from the Fermi energy, green for static peaks, and blue for peaks that move closer together. (Since eigenvalues repel at crossing points, this does not imply that the eigenvalues themselves follow straight lines.) Typically we find that the level broadening Γ_i of the peaks lying on the red lines are smaller than those of peaks lying on the blue lines.

To understand the nature of these resonances, we calculated the local density of states (LDOS) for two representative peaks lying on the blue and red trajectories. As an example, we focus on the system with an axial strain of 0.60, where the peaks are well separated. We employ SIESTA to calculate the LDOS for two energy ranges: $E-E_F=-0.05$ to $E-E_F=0.1$ and $E-E_F=0.45$ and $E-E_F=0.6$. These ranges are shaded in the bottom panel of figure 3 (a). Figure 3 (c) shows the resulting LDOS, as a function of axial position, averaged in the plane perpendicular to the transport direction. We see that the state associated with the blue-line peak is distributed over the full length of the region occupied by the TNT, whereas the state associated with the red-line peak is mostly localised on the leads. This indicates why the red-line peaks are typically narrower than the blue-line peaks, since their DOS is more localised and therefore their effective coupling of the leads is smaller.

To study the impact of mechanical deformations on the thermoelectric properties of the TNJs, we calculate the electrical conductance G , the Seebeck coefficient S , the thermal conductance κ_e and the electronic contribution to the figure of merit, ZT , for each axial strain configuration. These coefficients are given by^{12,30}

$$G = \frac{2e^2}{h} L_0, \kappa_e = \frac{2}{hT} (L_2 - \frac{L_1^2}{L_0}), S = -\frac{1}{|e|T} \frac{L_1}{L_0} \text{ and } ZT = \frac{L_1^2}{L_0 L_2 - L_1^2}, \text{ where}$$

$$L_n = \int_{-\infty}^{\infty} dE (E - E_F)^n T(E) \frac{\partial f(E)}{\partial E}. \quad (3)$$

(The above expression for S reduces to equ. (1) at sufficiently low temperatures.) In this expression, T is temperature, h is Planck's constant, and $f(E)$ is Fermi function. For the (3,3) TNT under axial strain, figures 4 (a-c) show results for G , ZT and S , while figure 4d shows the room-temperature Seebeck coefficient as a function of axial strain. The latter changes from positive to negative at a 0.53 and demonstrates that TNTs can exhibit bi-thermoelectricity. As shown by Figs. A1-A4 of the appendix, the (4,4) and (5,5) TNJs show similar bi-thermoelectric behavior.

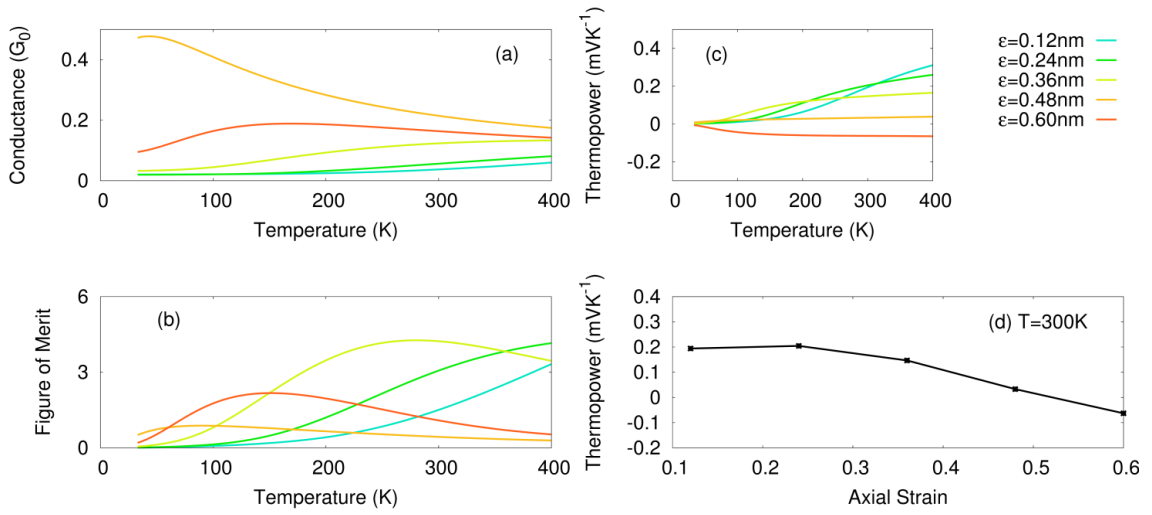


Figure 4. (a) The thermally averaged conductance, (b) the electronic contribution to the figure of merit and (c) the thermopower (ie Seebeck coefficient) against temperature for the (3,3) TNJ. (d) The room-temperature Seebeck coefficient against the axial strain. The precise value of the conductance depends on the location of the transmission peaks in figure 3a. The peak closest to the Fermi energy occurs for epsilon = 0.48, which is why this has the highest conductance in figure 4a. Note that in figure 3a, the scale is logarithmic, whereas a linear scale is used in figure 4a.

Conclusion

We have demonstrated that the thermoelectric properties of tapered carbon nanotubes can be tuned by the application of strain, which modifies the transmission coefficient of electrons passing through the strained tapered region. With increasing strain, the transmission resonances pass through the Fermi energy E_F of the electrodes, causing the slope of the transmission function $T(E_F)$ to switch sign, thereby changing the sign of the Seebeck coefficient. This bi-thermoelectric behaviour is desirable, since materials exhibiting Seebeck coefficients of alternating sign can be used in tandem thermoelectric devices to boost the thermovoltage³¹. One could of course change the sign of S by electrostatic gating. [insert refs] However this requires the expenditure of electrical energy and since the aim of a thermoelectric material is to scavenge energy efficiently, electrostatic tuning of S is not necessarily of technological benefit.

Acknowledgements

This work was supported by the European Commission (EC) FP7 ITN “MOLESCO” project no. 606728, UK EPSRC, (grant nos. EP/K001507/1, EP/J014753/1, EP/H035818/1)

References

1. Baheti, K. *et al.* Probing the Chemistry of Molecular Heterojunctions Using Thermoelectricity. *Nano Lett.* **8**, 715-719 (2008).
2. Yee, S.K., Malen, J.A., Majumdar, A. & Segalman, R. Thermoelectricity in Fullerene Metal Heterojunctions. *Nano Lett.* **11**, 4089 (2011).
3. Lee S. K., Ohto, T., Yamada, R. & Tada, H. Thermopower of Benzenedithiol and C₆₀ Molecular Junctions with Ni and Au Electrodes. *Nano Lett.* **14**, 5276 (2014).
4. Malen, J. A. *et al.* Identifying the Length Dependence of Orbital Alignment and Contact Coupling in Molecular Heterojunctions. *Nano Lett.* **9**, 1164-1169 (2009).

5. Tan, A. *et al.* Effect of Length and Contact Chemistry on the Electronic Structure and Thermoelectric Properties of Molecular Junctions. *J. Am. Chem. Soc.* **133**, 8838–8841 (2011).
6. Balachandran, J., Reddy, P., Dunietz, B. D., Gavini, V. End-Group-Induced Charge Transfer in Molecular Junctions: Effect on Electronic-Structure and Thermopower. *J. Phys. Chem. Lett.* **3**, 1962–1967 (2012).
7. Widawsky, J. R. *et al.* Length-Dependent Thermopower of Highly Conducting Au-C Bonded Single Molecule Junctions. *Nano Lett.* **13**, 2889–2894 (2013).
8. Chang, W. B. *et al.* Controlling the Thermoelectric Properties of Thiophene-Derived Single-Molecule Junctions. *Chem. Mater.* **26**, 7229–7235 (2014).
9. Evangeli, C. *et al.* Engineering the Thermopower of C₆₀ Molecular Junctions. *Nano Letters* **13**, 2141-2145 (2013).
10. Kim, S., Jeong, W., Kim, K., Lee, W. & Reddy, P. Electrostatic control of thermoelectricity in molecular junctions. *Nature Nano.* **9**, 881 (2014).
11. Zhang, Q., Sun, Y., Xu W. & Zhu, D. Organic Thermoelectric Materials: Emerging Green Energy Materials Converting Heat to Electricity Directly and Efficiently. *Adv. Mater.* **26**, 6829-6851 (2014).
12. Finch, C. M., García-Suárez, V. M. & Lambert, C. J. Giant thermopower and figure of merit in single-molecule devices. *Phys. Rev. B* **79**, 033405 (2009).
13. Bergfield, J. P., Solis, M. A. & Stafford, C. A. Giant thermoelectric effect from transmission supernodes. *ACS Nano* **4**, 5314–5320 (2010).
14. Snyder, G. J. & Toberer, E. S. Complex thermoelectric materials. *Nature Mater.* **7**, 105-113 (2008).
15. Harman, T. C., Taylor, P. J., Walsh, M. P. & LaForge, B. E. Quantum Dot Superlattice Thermoelectric Materials and Devices. *Science* **297**, 2229-2232 (2002).

16. García-Suárez, V. M., Lambert, C. J., Manrique, D. Z. & Wandlowski, T. Redox control of thermopower and figure of merit in phase-coherent molecular wires. *Nanotechnology* **25**, 205402 (2014).
17. Vacek, J., Vacek Chocholoušová, J. Stará, I. G., Starý, I. & Dubi, Y. Mechanical tuning of conductance and thermopower in helicene molecular junctions. *Nanoscale* **7**, 8793-8802 (2015).
18. Rincón-García, L., Ismael, A.K., Evangeli, C., Grace, I., Rubio-Bollinger, G., Porfyrakis, K., Agraït, N., and Lambert, C.J., Molecular design and control of fullerene-based bi-thermoelectric materials, *Nature Materials*, **15**, 289–293 (2016)
19. Sadeghi, H., Sangtarash, S., Lambert, C. J., Oligoyne molecular junctions for efficient room temperature thermoelectric power generation, *Nano Lett.* **15** (11), 7467-7472 (2015)
20. Paulsson, M. & Datta, S. Thermoelectric effect in molecular electronics. *Phys. Rev. B* **67**, 241403(R) (2003).
21. Ruoff, R. S. & Ruoff, A. L. The bulk modulus of C₆₀ molecules and crystals: A molecular mechanics approach. *Appl. Phys. Lett.* **59**, 1553 (1991).
22. L. Algharagholy, S.W.D. Bailey, T. Pope and C.J. Lambert, *Phys. Rev. B* **86** 075427 (2012)
23. L Algharagholy, T Pope, SWD Bailey, CJ Lambert, *New Journal of Physics* **16** (1), 013060 (2014)
24. Soler, J. M. , Artacho, E., Gale, J. D., García, J. Junquera, A., Ordejón P. and Sánchez-Portal, D. *J. Phys: Condensed Matter*, **14**, 2745 (2002).
25. Perdew, J. P., Burke K. and Ernzerhof, M. *Phys. Rev. Lett.*, **77**, 3865 (1996).
26. Ferrer, J. *et al.* GOLLUM: a next-generation simulation tool for electron, thermal and spin transport. *New J. Phys.* **16**, 093029 (2014).
27. Guinea, F., Katsnelson, MI. and Geim, AK. Energy gaps and a zero-field quantum Hall effect in graphene by strain engineering. *Nature Physics*, **6**(1):30–33, (2010).

28. Zhu, S., Stroschio, J.A. and Li, T. Programmable Extreme Pseudomagnetic Fields in Graphene by a Uniaxial Stretch. *Phys. Rev. Lett.*, **115**(24):245501, (2015).
29. Heyd, R., Charlier, A. and McRae, E. Uniaxial-stress effects on the electronic properties of carbon nanotubes. *Phys. Rev. B*, **55**(11):6820, (1997).
30. Lambert, C. J. Basic concepts of quantum interference and electron transport in single-molecule electronics. *Chem. Soc. Rev.* **44**, 875-888 (2015).
31. Benenti, G., Casati, G., Saito K. and Whitney, R.S. Fundamental aspects of steady-state conversion of heat to work at the nanoscale, *Phys. Rep.* **694**, 1 (2017).
32. Chen, X., Liu, Y., Gu, B-L., Duan, W. and Liu, F. *Phys. Rev. B* **90**, 121403(R) (2014)

Appendix

Strain-induced bi-thermoelectricity in tapered carbon nanotubes

L.A.A. Algharagholy^{1,3}, T. Pope², and C.J.Lambert¹

A. Breit-Wigner Fitting parameters

The Breit-Wigner model is fitted to the transmission coefficient data using a nonlinear least squares Marquardt-Levenberg algorithm. Table 1 shows the resulting parameters. For each fit, the 18 parameters were fitted to 240 data points.

	ϵ	$i = 1$	$i = 2$	$i = 3$	$i = 4$	$i = 5$	$i = 6$
ϵ_i	0.12	-0.19	0.37	-0.47	-0.15	0.42	0.26
	0.24	-0.23	0.41	-0.41	-0.10	0.39	0.28
	0.36	-0.27	0.45	-0.37	-0.06	0.36	0.30
	0.48	-0.32	0.49	-0.32	-0.01	0.33	0.28
	0.60	-0.38	0.52	-0.28	0.02	0.28	0.24
Γ_i	0.12	0.018	0.007	0.008	0.007	0.002	-0.009
	0.24	0.020	0.007	0.005	0.006	0.003	0.019
	0.36	0.020	0.006	0.005	0.005	0.004	0.035
	0.48	0.019	0.005	0.004	0.004	0.006	0.018
	0.60	0.016	0.005	0.004	0.003	0.009	-0.014
A_i	0.12	1.17	1.00	0.30	0.71	0.60	0.01
	0.24	1.00	0.96	0.43	0.92	0.80	0.03
	0.36	1.01	0.98	0.57	0.98	0.93	0.07
	0.48	0.94	0.99	0.86	0.99	0.93	0.20
	0.60	0.99	0.99	0.93	0.96	0.57	0.52

B. Results for the thermoelectric properties of (3,3), (4,4) and (5,5) TNJs.

Below, for the (3,3), (4,4) and (5,5) TNJs, we plot the electrical conductance and the electronic component of the figure of merit as a function of temperature, and the Seebeck coefficient as both a function of temperature, and as a function of axial strain at a constant temperature.

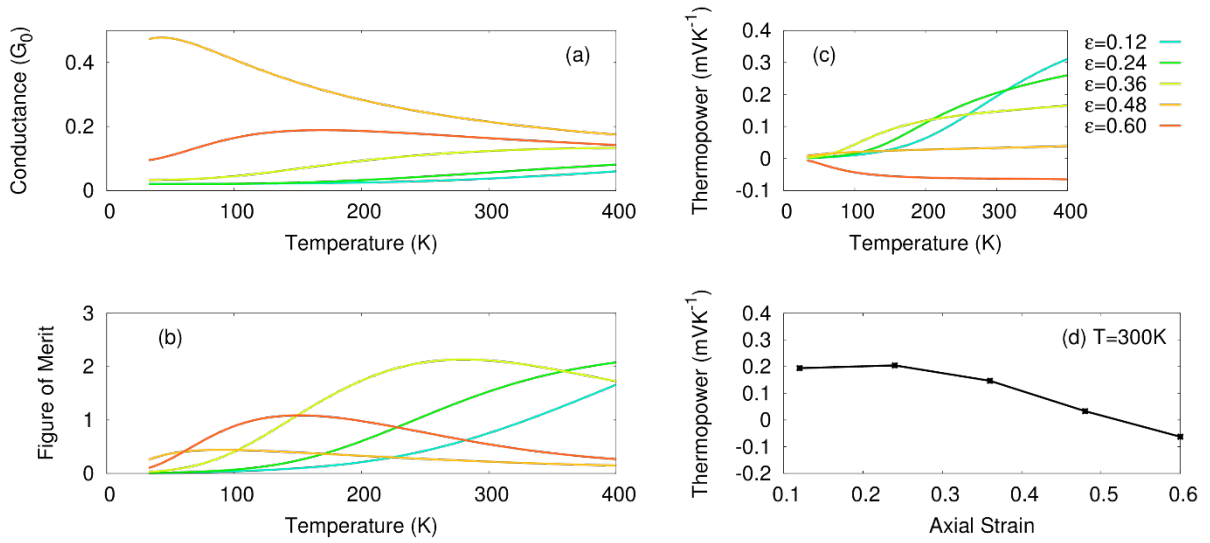


Figure A1: (a) Electrical conductance as a function of temperature for the (3,3)-junctions for a range of axial strain. (b) Electronic component of the figure of merit as a function of temperature for the (3,3) junction over a range of axial strain. (c) Thermopower (ie Seebeck coefficient) as a function of temperature for the (3,3) junction over a range of axial strain. (d) Seebeck coefficient at 300K as a function of axial strain for the (3,3) junction

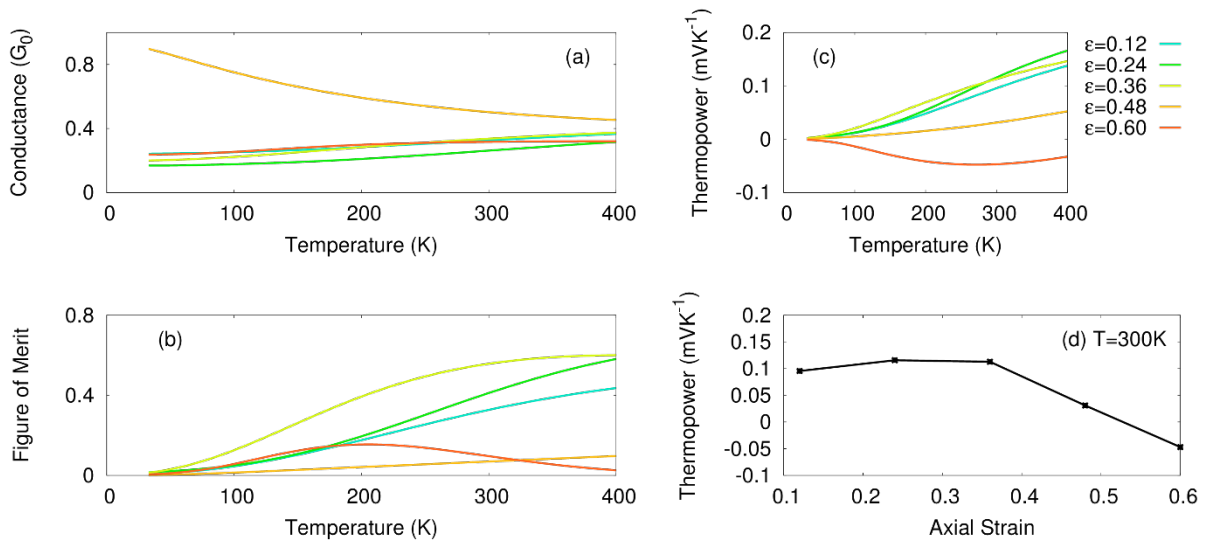


Figure A2: (a) Electrical conductance as a function of temperature for the (4,4) junctions for a range of axial strain. (b) Electronic component of the figure of merit as a function of temperature for the (4,4) junction over a range of axial strain. (c) Seebeck coefficient as a function of temperature for the (4,4) junction over a range of axial strain. (d) Seebeck coefficient at 300K as a function of axial strain for the (4,4) junction

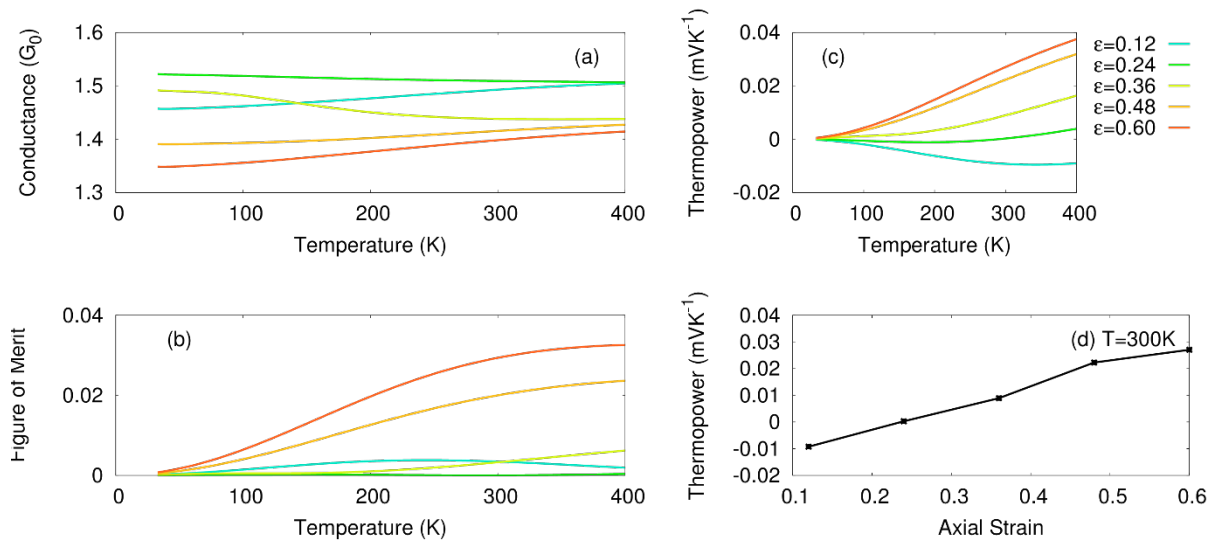


Figure A3: (a) Electrical conductance as a function of temperature for the (5,5) junctions for a range of axial strain. (b) Electronic component of the figure of merit as a function of temperature for the (5,5) junction over a range of axial strain. (c) Seebeck coefficient as a function of temperature for the 55-junction over a range of axial strain. (d) Seebeck coefficient at 300K as a function of axial strain for the (5,5) junction

For ease of comparison, the following figure shows the Seebeck coefficient as a function of axial strain. We note that while for low axial strain the thinner junction exhibit a higher thermopower, at higher axial strain the relationship is reversed, so that the thinner junctions has a lower Seebeck coefficient. The cross-over point is at $\epsilon=0.5nm$.

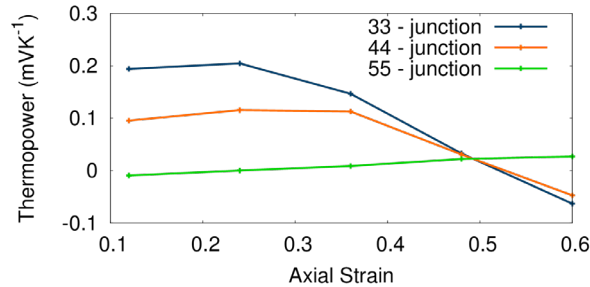


Figure A4: Seebeck coefficient at 300K as a function of axial strain for the three junctions.